

An appraisal of recent earthquake activity in Palghar region, Maharashtra, India

D. Srinagesh*, Dhiraj Kumar Singh, G. Vikas, B. Naresh, Sunil Roy, Y. V. V. B. S. N. Murthy, P. Solomon Raju, G. Suresh, Prantik Mandal, A. N. S. Sharma, M. Shekar and V. M. Tiwari

CSIR-National Geophysical Research Institute, Hyderabad 500 007, India

The present study focuses on the recent earthquake activity in Palghar region, Maharashtra, India. Until 31 August 2019, a total of 4854 earthquakes have been located here, whose local magnitude (M_L) varied from 0.1 to 4.1. Majority of the earthquakes (~94%) were located in the depth range 4–16 km. The precise earthquake relocations reveal two clusters. The N–S trending cluster north of 20.04°N extends to a depth of 10 km, whereas the NE–SW trending cluster to the south of 20.04°N extends to 16 km depth. The shallow northern cluster is noticed to be sandwiched between two mapped mafic intrusions, whereas the deeper southern segment shows earthquakes clustering around the mafic intrusion. The modelled composite focal mechanism solutions for both the north and south clusters suggest normal faulting with a minor strike–slip component as the dominant deformation mode for the Palghar region. From relocated seismicity, we have detected a deeper seismically active zone (with $M > 3$) at 4–16 km depth, occupying a crustal volume of 1440 km³ (i.e. 20 km (in N–S) × 6 km (in E–W) and 12 km (in depth)) that dips toward 20°S and 70°W. This could be attributed to the large crustal stresses induced by the mafic intrusive body below the region.

Keywords: Crustal stress, deformation mode, earthquake, mafic intrusion, relocations, seismic activity.

THE east and west coasts of India are passive continental margins evolved as a consequence of the country rifting with eastern Antarctica, Madagascar and Seychelles^{1,2}. The Palghar seismic sequence about 100 km north of Mumbai, Maharashtra, India began on 11 November 2018 with the activity confined between the Western Ghats escarpment and the NW–SE trending west coast fault (Figure 1). The Deccan traps are the predominant geology with a number of mafic intrusions mapped. These intrusions are oriented either in the N–S or NW–SE directions, with two of them located in the vicinity of the seismic activity³.

Spatial distribution of epicentres provides information about the tectonic regime and disposition of the source

zone in three dimensions. Earthquake hypocentres need to be precisely located together with the velocity structure in order to understand the causative factors of earthquake activity. Minimization of uncertainty in the hypocentral parameter estimates is mainly governed by the Azimuthal gap (GAP) without P - or S -wave arrival times observation, which needs to be less than 180° (ref. 4), the number of P - and S -wave arrival times and accuracies in their pick-up⁵ and finally the closest seismological station contributing to the S -wave arrival time⁶. CSIR-NGRI deployed six broadband seismological stations and one accelerograph to monitor the ongoing earthquake activity in Palghar district; the complete network has been functional from 30 January 2019. Figure 1 shows the network configuration and Table 1 provides the details thereof. Each seismic station is equipped with a 24-bit Reftek data acquisition system coupled with CMG-3C broadband seismometers at two locations and REFTEK 151 broadband seismometers at four locations. The minimum GAP of the network configuration is about 100°. Data were recorded at 100 samples per second (sps) with earthquake data processed in near real-time for

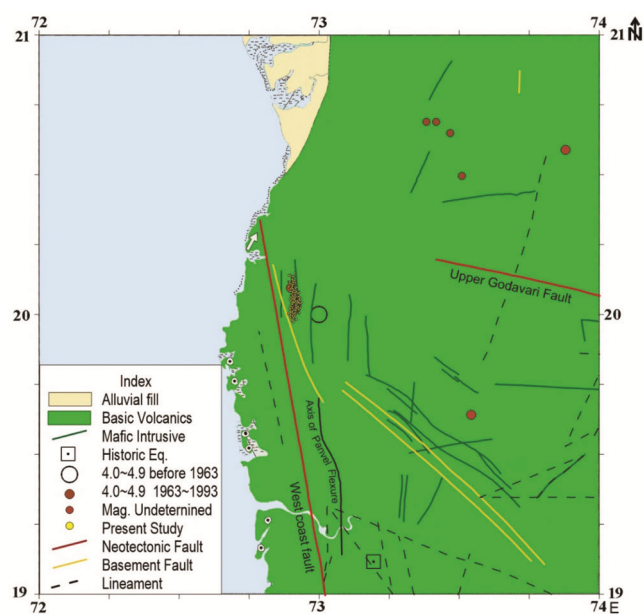


Figure 1. Recent seismicity and seismo-tectonics of the study region⁷.

Table 1. List of six broadband seismographs in the Palghar region, Maharashtra, India

Station code	Latitude (°N)	Longitude (°E)	Elevation (m)
KAWA	20.1167	72.8851	47
UDHW	20.0945	73.0026	62
KAIN	20.0241	72.7748	44
AINE	19.8943	72.8423	50
GAGO	19.9867	73.0282	113
MASA	20.1908	72.9428	43

*For correspondence. (e-mail: srinagesh@ngri.res.in)

determining hypocentral parameters, while time-tagging was done with a GPS receiver having accuracy in microseconds. The data recorded (at 100 sps) has allowed us to pick *P*- and *S*-wave phases with an accuracy of 0.02 and 0.05 sec respectively. Precise *S*-wave arrival times were obtained from the transverse component of the rotated seismograms. The network geometry was carefully designed to fulfil the criteria suggested by Gomberg *et al.*⁶, with the nearest station located at a distance of less than 1.4 times the focal depth for which the *S*-wave phase arrival times have been used in determining the hypocentral parameters.

Sporadic seismic activity in the past has been reported around the current activity with m_b 4.1 earthquake of 21 June 1989 being reported till date (source: ISC, UK) (Figure 1). However, there are no reports of large earthquake occurrences in the recent past, except a few of magnitude ranging from 4.0 to 4.9 reported before 1993 (ref. 7) (Figure 1). About 20 km SE of the current activity, reservoir-triggered seismicity was reported at the Dhamni reservoir, which began in 1984 and continued up to 1986. The seismic activity paused and got reactivated in 1994, continuing up to 1995. During this period, the CSIR-NGRI seismological network recorded more than 4785 earthquakes ranging between 0.0 and 2.9, of which 69 had magnitude > 3.0 .

Until 31 August 2019, three-component seismological waveforms of 4854 earthquakes have been analysed for *P*- and *S*-wave arrival time picks with local magnitude (M_L) ranging from 0.1 to 4.1. Prior to the inversion of travel-time data, Wadati analysis was carried out by plotting *S*-*P*-wave travel time differences versus *P*-wave arrival times for estimating the V_p/V_s value (1.73; Figure 2). The V_p/V_s value is important for obtaining the *S*-wave velocities for the initial velocity model. Seisan software version 11 was used in preprocessing the earthquake waveforms and initial hypocentral parameters were obtained using HYPOCENTER program, which is built in the Seisan software⁸. The velocity model (Table 2) proposed from the DSS results for Koyna Profile II was used as the initial model in locating earthquakes^{9,10}. The focal depths were determined by plotting RMS with different trial depths (Figure 3 *a-f*) and the final estimated focal depth was selected as the one showing minimum RMS. The estimated RMS errors in the initial locations varied from 0.01 to 0.19 sec (Figure 3 *g*), with a mean of 0.05 sec. The mean errors in initial epicentral location and focal depths were 1.0 and 2.0 km respectively, for the Palghar earthquakes. Figure 4 *a* shows the epicentral plot of the initial locations of 4854 earthquakes. The seismicity can be discriminated into two clusters, i.e. north and south. The N-S and E-W depth sections of hypocentres reveal a southwest-dipping seismic zone, occupying a crustal volume of 11 km (in N-S) \times 4 km (in E-W) \times 15 km (in depth) (Figure 4 *b* and *c*). The N-S cross-section suggests a 20°S dip of the seismic zone, while

E-W cross-section reveals a 70°W dip. Both N-S and E-W depth sections suggest the occurrence of very shallow clusters of smaller events ($M < 3$) at 0–2 km depth (Figure 4 *b* and *c*). The change in the bipolar Regional Bouguer gravity anomaly along 20°N profile shown in Figure 4 *d*, coincides with the zone of seismic activity.

The initially determined hypocentral locations were simultaneously inverted using VELEST code to estimate both the 1D velocity structure and earthquake relocations¹¹ (Figure 5 *a-e* and Table 3). The initial ten-layer V_p and V_s crustal models were constructed using the above-mentioned four-layer velocity model (dotted lines in Figure 5 *e*), which was used to obtain the initial locations of earthquakes. The 1D *P*- and *S*-wave velocity models were estimated by inverting for velocity model and epicentral locations. The centre location for the simultaneous inversion of Palghar data was 20.05°N, 72.91°E. Figure 5 *e* and Table 3 show the initial and final 1D V_p and V_s models. The V_p/V_s ratio from the inverted velocity model was about 1.73 and correlated well with the Wadati analysis values (Figure 2). The final inverted velocity model was used to relocate 4854 events of M_L 0.1–4.1, using 23,659 *P*-wave and 22,468 *S*-wave arrival times as input data.

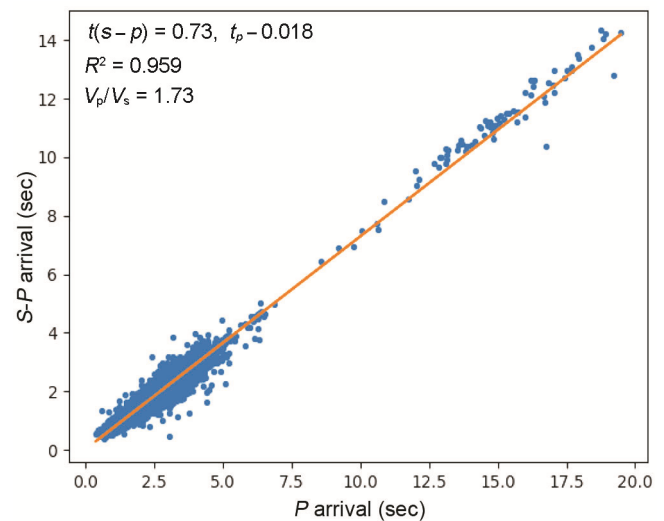


Figure 2. Wadati plot of arrival times of *P*-waves (i.e. $t_p(s)$), and differences between arrival times of *P*- and *S*-waves (i.e. $t(s-p)(s)$) for 4854 Palghar events of M_L 0.1–4.1, which occurred during January–August 2019.

Table 2. Velocity model used for locating earthquakes

Depth to top of the layer	Initial velocity model	
	V_p (km/sec)	V_s (km/sec)
0.0	4.95	2.86
1.0	6.20	3.58
20.5	6.60	3.81
30.0	6.90	3.99
37.0	8.26	4.77

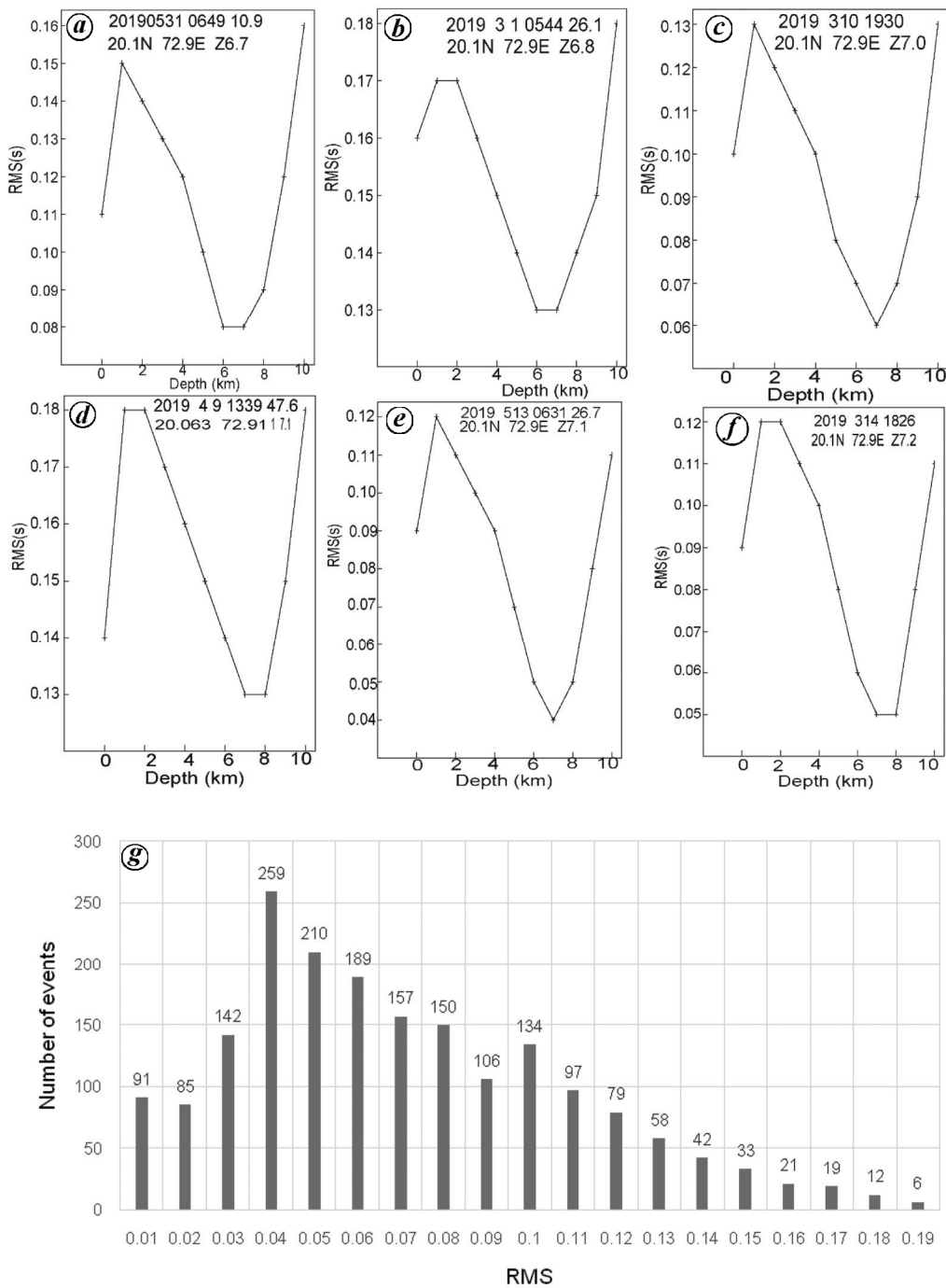


Figure 3 a-f. RMS versus trial depths plot for six earthquakes to estimate the best focal depth with a minimum RMS. **g,** Histogram of estimated RMS for different earthquakes, showing average RMS of 0.05 for all located earthquakes.

The mean epicentral error on earthquake relocation was found to be 150 m, while the mean error in focal depth was estimated as 250 m. The Figure 5 a distinctly shows that the earthquakes are clustered into two zones. One cluster is associated with shallow events in the north, while the second cluster is associated with the deeper events in the south. The N–S depth section of the relocated hypocentres delineates a seismic zone dipping

toward 20°S extending from 4 to 16 km depth. The vertical line (AA') in Figure 5 b separates the shallow north cluster from the deeper south cluster. While Figure 5 c shows the E–W depth section of relocated hypocentres suggesting a 70°W dipping seismic zone covering an area of 6 km extending from 4 to 16 km depth. Both N–S and E–W depth cross-sections show a cluster of some very shallow smaller events ($M < 3$) at 0–2 km depths, which

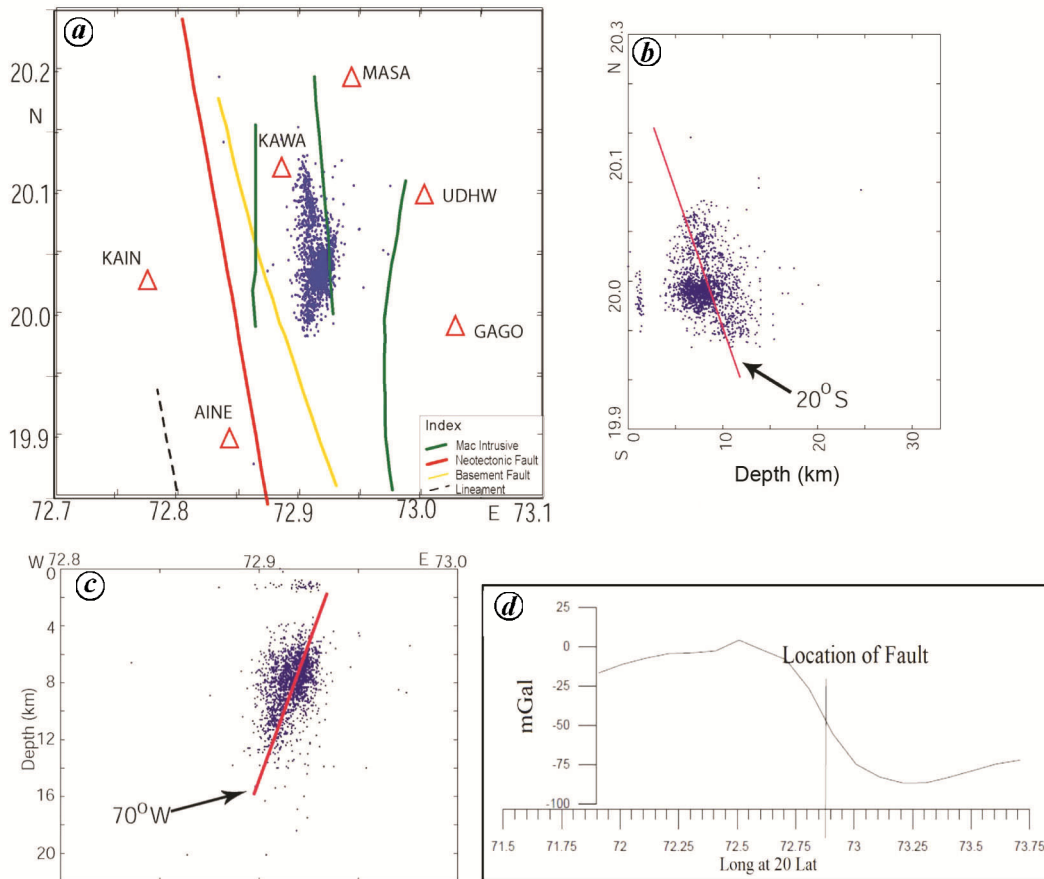


Figure 4. *a*, Spatial distribution of initial epicentral locations of 4854 Palghar events of M_L 0.1–4.1 using SEISAN. Blue dots mark the epicentres and red open triangles represent broadband seismographs. *b*, N–S depth plot of hypocentres. The thick red line shows the 20°S dipping seismic zone. *c*, E–W depth plot of hypocentres. The red line shows the 70°W dipping seismic zone. *d*, Regional Bouguer gravity profile showing location of the fault.

Table 3. Initial and final *P*- and *S*-wave velocity models

Depth to top of the layer	Initial velocity model		Final velocity model	
	V_p (km/sec)	V_s (km/sec)	V_p (km/s)	V_s (km/s)
0.0	4.95	2.86	5.125	2.771
1.0	6.20	3.58	5.906	3.572
3.0	6.20	3.58	6.125	3.579
5.0	6.20	3.58	6.197	3.619
7.0	6.20	3.58	6.561	3.724
10.0	6.20	3.58	6.591	3.757
15.0	6.20	3.58	6.598	3.760
20.0	6.60	3.82	6.623	3.827
33.0	6.90	3.99	6.900	3.990
37.0	8.26	4.78	8.260	4.780

seems to be decoupled from the main seismic cluster at 4–16 km depth, as mentioned above. This bimodal depth distribution of seismicity is also seen clearly from the 3D plot of seismicity using ZMAP¹² (Figure 5 *d*).

Majority of earthquakes (94%) were located within the upper crust of 4–16 km depth (Table 4). Seismicity plots revealed two distinct clusters. Twenty-two earthquakes of

M_L 3 and above occurred during 30 January 2019 to 24 March 2019, with the largest (M_L 4.1) occurring on 1 March 2019. The intensity survey was carried out during 6–9 February 2019, since eight earthquakes of magnitude M_L 3.1–3.7 occurred on 1 February 2019 in a span of 8 h. The intensities were estimated on modified Mercalli scale based on the observations and the effects of intense

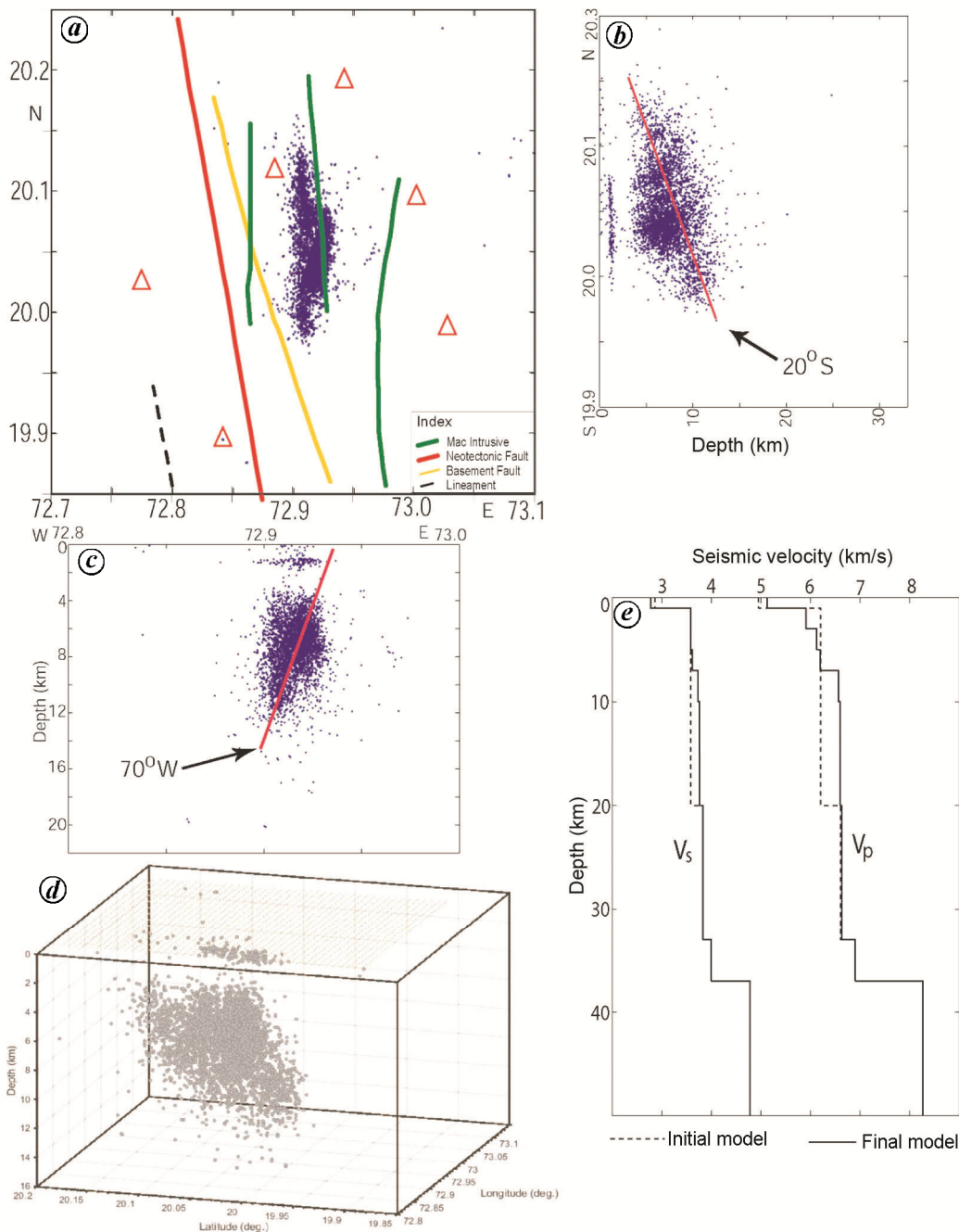


Figure 5. *a*, Spatial distribution of relocations of 4854 Palghar events of M_L 0.1–4.1 using Velest code. The grey square marks the shallow north cluster, while the grey elliptical area marks the deeper south cluster. Blue dots mark the epicentres and red open triangles represent broadband seismographs. *b*, N–S depth plot of hypocentres. The thick red line shows the 20°S dipping seismic zone while the grey line separates the shallow north cluster from the deeper south cluster. *c*, E–W depth plot of hypocentres. The red line shows the 70°W dipping seismic zone. *d*, 3D plot of relocated seismicity (Zmap software)¹². *e*, Plot showing the initial (solid grey line) and final (dotted grey line) P - and S -wave velocity models for the present 1D travel time inversion study using Velest code.

ground shaking. The isoseismals were elliptical in shape and the zone of maximum intensity of V coincided with the location of magnitude 3 earthquakes and reported intense ground shaking, while at 10 km distance from the maximum the intensity decreased to II.

We determined composite focal mechanisms from the first-motion data plotted on the lower hemisphere of equal-area projection for the northern and southern seis-

micity clusters separately (Figure 6 *a* and *b*). Figure 6 shows the azimuth, dip and rake of both the nodal planes for the above-mentioned two composite focal mechanism solutions. Any one of the nodal planes trending N–S or NNE–SSW could be the fault plane. Here, we prefer the NNW–SSE trending plane as the fault plane for the northern seismicity cluster which also suggests normal faulting with a minor strike–slip component on a plane

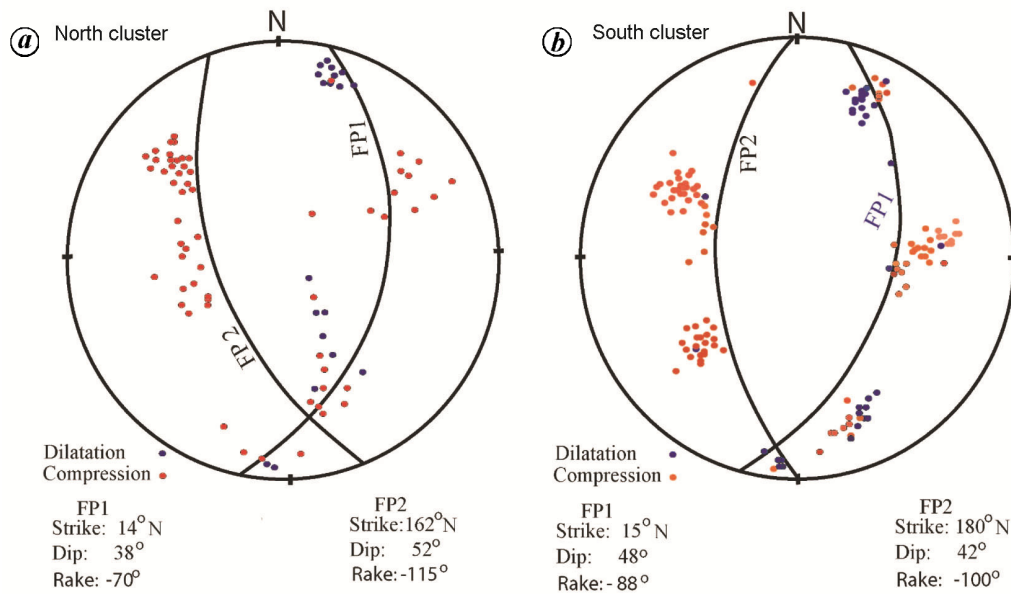


Figure 6. Composite focal mechanism solutions for (a) north cluster and (b) south cluster of seismicity. Both the solutions suggest a normal faulting with minor strike-slip component as the dominant deformation mode for the Palghar region.

Table 4. Frequency of occurrence of earthquakes at different depth ranges

Focal depth range (km)	No. of earthquakes
0–1.99	181
2.0–3.99	116
4.0–5.99	983
6.0–9.99	3015
10.0–20.0	559

steeply ($\sim 52^{\circ}$) dipping towards the southwest (Figure 6a). While we consider the NS trending plane as the fault plane for the southern cluster of seismicity, which suggests normal faulting with a minor strike-slip component on a plane steeply ($\sim 48^{\circ}$) dipping towards the west (Figure 6b). The estimated *P*-axis (maximum compression) for the northern cluster suggests a nearly NE–SW orientation while *T*-axis shows an E–W orientation. However, the estimated *P*-axis (maximum compression) for the southern cluster suggests a nearly NE–SW orientation, while *T*-axis shows an E–W orientation. We found at least 10% inconsistent observations of first motion, thus the orientation of the nodal planes could be off by about 10° in dip as well as strike.

Relocated seismicity (Figure 5a) reveals fault segmentation with seismicity cluster to the north of 20.04°N , oriented the N–S direction and extending up to 10 km depth. The dense cluster of seismicity to the south of 20.04°N is oriented in the NE–SW direction with focal depth extending down to 16 km (Figure 5b). The northern segment is confined between the two mafic intrusions whereas the southern segment characterized by dense clustering of earthquakes is straddling around the mafic intrusion (Figure 5b). The Regional Bouguer gravity

anomaly profile along 20°N (Figure 4c) shows a change in the polarity of the anomaly, indicating that the causative feature is deep-seated, which is supported by the depth distribution of earthquakes. The 3D plot of seismicity using ZMAP¹² (Figure 5d), shows two clusters of hypocentres, i.e. a shallow cluster at 0–2 km depth and a deeper southwest-dipping cluster at 4–16 km depth. This deeper cluster is inferred as the main cluster of seismicity. Analysing the relocated seismicity plotted in Figure 5a–d, we have detected a deeper seismically active zone at 4–16 km depth, occupying a crustal volume of 1440 km^3 (i.e. 20 km (in N–S) \times 6 km (in E–W) and 12 km (in depth)) that dips towards 20°S and 70°W . Thus, this deeper seismicity with events of $M > 3$ could be related to the mafic intrusive body below the region, as also mapped by surface geological information (Figure 5a). However, we also detected a shallow cluster of seismicity ($M < 3$) at 0–2 km depth, which has been decoupled from the main seismic zone at 4–16 km depth. This shallow cluster needs to be examined in greater detail.

The composite focal mechanisms have been determined for the northern and southern clusters of seismicity. The estimated composite focal mechanism solutions reveal normal faulting with a minor strike-slip component on a NNW–SSE trending plane steeply ($\sim 52^{\circ}$) dipping towards the southwest for the northern seismicity cluster. The deformation mode in the southern seismicity cluster is found to be characterized by normal faulting with a minor strike-slip component on a plane steeply ($\sim 48^{\circ}$) dipping towards the west (Figure 6a and b). Thus, the present study suggests domination of normal faulting or extensional stress regime in the Palghar area. It is noteworthy to mention that the western part of India has rifted from Madagascar during 85 Ma and Seychelles

later¹. Syn rifting of the Indian Plate from Seychelles and the Deccan Trap eruption were contemporaneous to the time when the Indian Plate passed over the La Reunion hotspot². The consequence of the Indian Plate rifting resulted in the horst and graben structure and a number of intrusions along the west coast passive margin, which is evident from several studies. Thus, we infer that large intraplate stresses associated with the upper crustal mafic intrusions along with the prevailing in-plane compression of the Indian Plate might have induced near to critical stressed regions for the pre-existing west-dipping or vertical normal faults in the region, which might have caused the genesis of earthquake sequence in the Palghar region. Geophysical studies like gravity, magnetics and magnetotellurics are in progress to understand the seismotectonics of this region.

1. Reeves, C. V. and de Wit, M., Making ends meet in Gondwana: retracing the transforms of the Indian Ocean and reconnecting continental shear zones. *Terra Nova*, 2002, **12**(6), 272–280.
2. Courtillot, V. E., Besse, J., Vandamme, D., Montigny, R., Jaeger, J. and Cappetta, H., Deccan flood basalts at the Cretaceous/Tertiary boundary? *Earth Planet. Sci. Lett.*, 1986, **80**, 361–374.
3. Deshpande, G. G. and Pitale, U. L., *Geology of Maharashtra*, Geological Society of India, 2014, pp. 1–265.
4. Kissling, E., Geotomography with local earthquake data. *Rev. Geophys.*, 1988, **26**, 659–698.
5. Chatelain, J. L., Roecker, S. W., Hatzfeld, D. and Molnar, P., Microearthquake seismicity and fault plane solutions in the Hindu Kush region and their tectonic implications. *J. Geophys. Res.*, 1980, **85**, 1365–1387.
6. Gombert, J. S., Shedlock, K. M. and Roecker, S. W., The effect of S-wave arrival times on the accuracy of hypocenter estimation. *Bull. Seismol. Soc. Am.*, 1990, **80**, 1605–1628.
7. Dasgupta, S. *et al.*, *Seismotectonic Atlas of India and its Environs*, Geological Survey of India, 2000.
8. Ottemoller, L., Voss, P. and Havskov, J., Seisan Earthquake Analysis Software, Version 11, 2018.
9. Kaila, K. L., Murthy, P. R. K., Rao, V. K. and Kharetchko, G. E., Crustal structure from deep seismic sounding along the Koyana II (Kelsi–Loni) profile in the Deccan Trap area, India. *Tectonophys.*, 1981, **73**, 365–384.
10. Kaila, K. L., Reddy, P. R., Dixit, M. M. and Lazarenko, M. A., Deep crustal structure at Koyana, Maharashtra, indicated by deep seismic sounding. *J. Geol. Soc. India*, 1981, **22**, 1–16.
11. Kissling, E., *Veles User's Guide*. Internal report, Institute of Geophysics, ETH Zürich, Switzerland, 1995, p. 26.
12. Wiemer, S., A software package to analyze seismicity: ZMAP. *Seismol. Res. Lett.*, 2001, **72**(3), 373–382.

ACKNOWLEDGEMENTS. We thank the Director, CSIR–NGRI, Hyderabad, for encouragement and permission to publish this work. We acknowledge the help rendered by district authorities in obtaining permissions and logistic support during seismic station network installation.

Received 3 April 2019; revised accepted 10 February 2020

doi: 10.18520/cs/v118/i10/1592-1598

Inheritance of fruiting habit traits in chilli (*Capsicum annum* L.)

C. Anilkumar*, A. Mohan Rao, S. Ramesh, B. Bhavani and Pranesh

Department of Genetics and Plant Breeding, College of Agriculture, University of Agricultural Sciences, Gandhi Krishi Vignana Kendra, Bengaluru 560 065, India

Fruiting habit, viz. fruits node⁻¹ and fruit orientation are economically important traits in chilli. Fruiting habit could be solitary erect, solitary pendant, clustered erect or clustered pendant. Farmers' preference for fruiting habit traits varies from region to region. An understanding of the inheritance of fruiting habit traits helps accelerate breeding chilli cultivars with farmer-preferred combination of such traits. Eight diverse genotypes contrasting for fruiting habit traits were crossed to develop ten F₁ hybrids of six combinations. The F₂ and backcross generations of all the six distinct types of crosses were evaluated and pattern of segregation for fruiting habit traits was recorded. Results indicated bi-allelic, monogenic inheritance of fruits node⁻¹ (solitary versus clustered) and fruit orientation (pendant versus erect) with solitary being dominant over clustered and pendant being dominant over erect orientation respectively. Genes controlling fruits node⁻¹ and orientation of fruits segregated independently. Implications of these results are discussed in relation to strategic and applied chilli breeding.

Keywords: Chilli, fruiting habit traits, goodness-of-fit, inheritance.

HOT pepper (*Capsicum annum* L.; $2n = 2x = 24$), popularly known as chilli in India, is an important economic crop worldwide¹, and is ranked second among Solanaceous vegetable crops after tomato². The species *Capsicum* originated in Mexico with centre of diversity in South America³. Presence of pepper-specific secondary metabolites – capsaicinoids – which confer pungency to fruits and possess various medicinal properties has made chillian important culinary item⁴. The fruits contain an appreciable quantity of nutrients, including ascorbic acid, β -carotene and other carotenoid pigments such as lycopene and zeaxanthin possessing anticancer properties⁵. India is the foremost producer and exporter of chilli, contributing to one-fourth of the world market share. Even though chillies are grown in all parts of the country, Andhra Pradesh, Karnataka, Odisha, Maharashtra, Rajasthan and Tamil Nadu are the major chilli-growing states in India, accounting for 80% of area and 84% of total production.

Fruit orientation and number of fruits node⁻¹ are fruiting habit traits which are economically important. Fruit

*For correspondence. (e-mail: anilegpb@gmail.com)